LU-TP 21-28
June 2021

Data Mapping Across Compact Cellular Tissues of Varying Morphology

Jonas Petersson

Department of Astronomy and Theoretical Physics, Lund University

Master thesis supervised by:

Victor Olariu, Lund University
Henrik Jönsson, University of Cambridge
Argyris Zardilis, University of Cambridge
Henrik Åhl, University of Cambridge

LUND
UNIVERSITY

Abstract

A problem with cellular image data from plant tissues is that it is difficult to compile and compare data from different specimens due to their varying morphology. In this thesis, a method for compiling image data from different tissues in a unified geometry is developed and evaluated on early floral buds of *Arabidopsis thaliana*. The proposed method can transfer subcellular resolution data between tissues on both cell and tissue scale. The images are first aligned on a tissue level using image registration techniques, and it is then possible to determine the cell-to-cell connections between the tissues. After the cell-to-cell connections have been found, the data is decomposed in a form that is easy to transfer between the images. By dividing the cells into sectors formed by angular intervals, it is possible to map data that is asymmetrically distributed across an individual cell's membranes. It is shown that hormone transport simulations based on the raw data and the mapped data of geometries and cell polarity have similar behaviours, indicating that the data distribution remains intact after the mapping. The method shows promise for revisiting older datasets and integrating them with new ones for improved analysis and model optimization.

Populärvetenskaplig Beskrivning

Vår kunskap om växter har ökat sedan den första jordbruksrevolutionen för mer än 10.000 år sedan, men det är fortfarande mycket vi inte vet. Med moderna mikroskop och genmodifieringstekniker har växtcellernas inre processer börjat kartläggas. Genom att använda fluorescerande markörer som är bundna till de protein man vill undersöka så kan man se var dessa proteiner finns på cellnivå. Ett problem är att man bara kan använda ett fåtal markörer i samma vävnad, och istället krävs flera separata vävnader med olika markörer. De separata vävnaderna gör det svårare att analysera datan eftersom de olika vävnaderna har varierande struktur och olika mängder celler med annorlunda former. Målet med denna uppsats är att utveckla en metod för att kunna integrera data från flera olika vävnadsprover, i en såkallad atlas.

Det första steget är att se till att vävnaderna har samma form. Detta kan illustreras med en bild på en amerikansk fotboll och en på en vanlig fotboll. Båda objekten är bollar, men de har olika form. Genom att manipulera bilden på den amerikanska fotbollen så kan man göra den mer sfärisk, så att om man skulle klippa ut bilden på den manipulerade amerikanska fotbollen och placera den på bilden av den vanliga fotbollen så skulle de överlappa perfekt. På samma sätt som man kan manipulera en bild på en fotboll så kan man manipulera en tredimensionell bild av en vävnad, så att flera vävnader får samma form. När vävnadsbilderna har manipulerats så de har samma form är det möjligt att sammanställa informationen i de olika vävnaderna.

I denna uppsats presenteras en ny metod för att överföra data mellan vävnader med varierande former. Metoden testas på bilder av blommor i ett mycket tidigt utvecklingsstadie från växten *Arabidopsis thaliana*. Efter att bilddatan har blivit manipulerad så att vävnaderna överlappar så är det möjligt att överföra data från den ena vävnaden till den andra. Genom att sedan göra simuleringar med både originaldatan och datan som är överförd till den andra vävnaden kan man jämföra om simuleringarna beter sig på samma sätt. Resultatet från simuleringarna visar att dynamiken kvarstår efter dataöverföringen, vilket indikerar att metoden lyckas med en form av dataöverföring som inte gjorts förr. Med hjälp av denna nya metoden kan gammal och ny data sammanställas i en form som möjliggör avancerade simuleringar och analyser.

Contents

List of acronyms

SAM - Shoot Apical Meristem
RAM - Root Apical Meristem
FM - Floral Meristem
SMD - Sectorial Mean Decomposition
LFY - LEAFY
AP1 - APETALA1
IAA - Indole-3-Acetic Acid
PIN - PIN-FORMED
GFP - Green Fluorescent Protein
SMD - Sectorial Mean Decomposition
LAX - Like-AUX

List of Figures

List of Tables

1 Introduction

Plant science and image analysis are tightly connected fields, where computational techniques are used to extract useful information from microscopy images. In images where cell membranes are distinguishable, it is possible to segment the image into labelled sub-regions corresponding to individual cells[1]. The segmented images enable analyses of growth and shape[2], as well as tracking of individual cell lineages[3]. When the images also contain data such as hormone abundance and gene expression, quantification techniques open up possibilities for mathematical models, which help test the understanding of biological systems[4, 5].

A common problem in computational plant biology is how to compile molecular data from different specimens. As more and more data is gathered, it is possible to represent the data in an atlas that contains information on different molecules' distributions throughout a representative tissue[6, 7, 8]. In addition, an atlas enables large-scale analyses of the interactions between molecules from different sources and simulations of their dynamics. Recently, the Plant Cell Atlas Initiative was started with the goal of creating a unified atlas for plant cells, from tissue level to molecular level[9]. One of the outstanding questions that the Plant Cell Atlas Initiative highlights is "How do plant cells establish and position functional domains at their periphery to regulate cytoskeletal organisation, morphogenesis, polarised intercellular communication, and developmental patterning?", which is a question that the method developed in this thesis helps to answer.

Compilation of cell data in, for example, a binary form can be made by combining information on whether a particular gene is expressed or not through manual inspection of multiple tissues and comparison of the expression levels in corresponding cells relative to some threshold[6]. However, the manual approach becomes problematic when the data is neither binary nor scalar and when the maintenance of the molecule's intracellular distribution is critical in the atlas. Another approach to comparing different samples is identifying and annotating certain cell types, which enables gene expression and cell geometry analysis[10], but not the compilation of multiple samples into a single geometry for simulation purposes. In this thesis, three main contributions are presented to solve the issues related to data compilation in an atlas.

The first contribution is a novel method, Sectorial Mean Decomposition (SMD), for mapping membrane-bound molecules while preserving intracellular distributions and cellular concentrations between cells. By decomposing the cells in sectors defined by angular intervals, it becomes possible to map heterogeneous data from cell to cell, even if their geometries are different. The second contribution is a unified workflow (Fig. 6), which includes the steps for the raw image data mapping to the geometry of the atlas tissue. The third contribution is the verification of the procedure by running simulations using the mapped data, which shows that the dynamics of the model is preserved after the mapping.

Currently, there is no available automatic procedure for the whole process of performing polar data mapping across compact tissues with varying morphology. However, with the

method presented in this thesis, it will be possible to revisit older data sets and integrate them with new data, enabling further analysis and improved models.

The background section will present necessary information about plants and image processing which the result and method section presumes. In the result section, the novel method, SMD, is evaluated when applied to flower primordia of *Arabidopsis thaliana*, and the focus is mainly on the steps carried out to evaluate the method. The method section presents technical details of the segmentation, registration technique, overlap calculations, and SMD. A brief description of the quantification and simulation method used is also included.

2 Background

2.1 The developing plant

Plants have adapted to grow differently compared to animals due to factors as their lack of muscles and their cells' general inability to move around the organism. This non-migratory behaviour has given rise to solutions to ensure that the plant is growing in the correct direction and that it can reorient its growth, e.g. given light conditions or if it would fall over. One way plants can change growth direction is through differential growth[11]; for example, if the cells in the stem grow slower on the left side than on the right side, the stem would start curving towards the left. The different ways in which a plant's growth is affected by various stimuli are referred to as positive tropism (towards stimulus) and negative tropism (away from the stimulus)[12]. Two common plant tropisms are gravitropism (response to gravity) and phototropism (response to light), both of which depend on a family of hormones called auxins[13]. Phototropism mainly affects the part of the plant above ground (the aerial part) through photoreceptors, and since plants typically need light, the aerial part experiences positive phototropism[14].

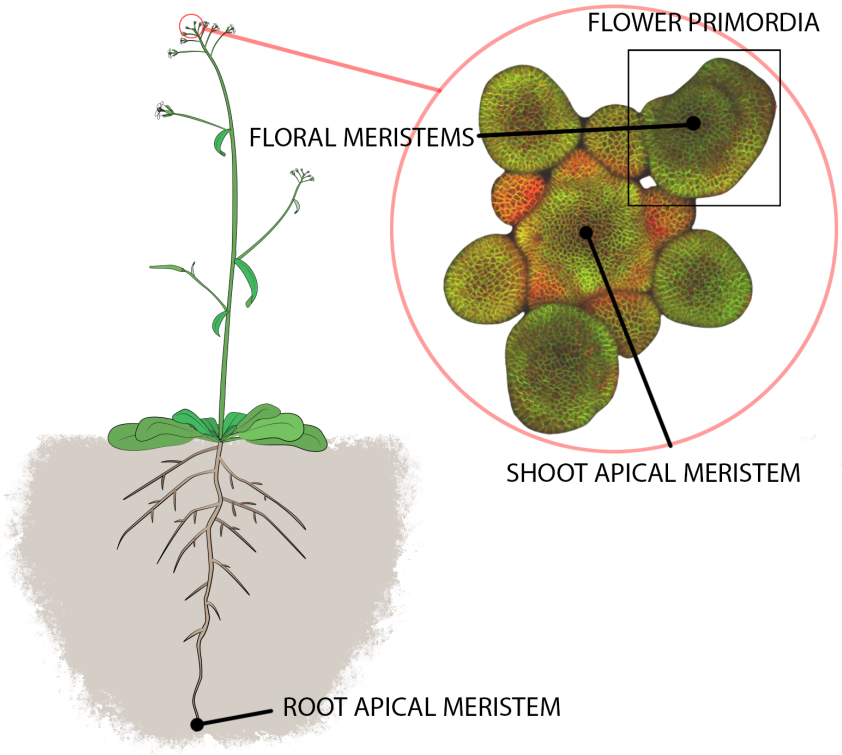

Figure 1: Schematic figure of *Arabidopsis thaliana* showing the location of a shoot apical meristem and a root apical meristem. Within the black square, a flower primordium is shown, with the central part being the floral meristem which is surrounded by sepal primordia. Several floral primordia in their early stages of development can be seen around the shoot apical meristem. The original drawing of the plant[15] shown here was modified to highlight the aerial portion of the plant, the image was also modified to include a zoomed in section of the SAM.

With the plants' aerial and underground sides separated, the sides are spearheaded by two regions of stem cells called the shoot apical meristem (SAM) and the root apical meristem (RAM)[16](Fig. 1). In the SAM, flower primordia with a central region called the floral meristem (FM) are formed[17], which develop into the plants' flowers (Fig. 2), and this is the tissue that will mainly be discussed in this thesis. It is also important to mention that the specific plant discussed in this thesis is *Arabidopsis thaliana*, a widely used model organism due to its small size, sequenced genome, fast growth, and large seed production[18].

The first step in the formation of the flower is the organ initiation, a process that can be identified by the formation of local peaks of auxin[19, 20] as well as the proteins LEAFY (LFY) and APETALA1 (AP1)[21, 22, 23, 24, 25] in the SAM. As the flower primordium begins to grow, the development can be divided into stages (Fig. 2) where the first four are the ones of interest in this thesis, and they can be summarised as follows[17]:

- Stage 1: A small outgrowth can be identified on the SAM.
- Stage 2: A groove is formed between the flower primordia and the SAM.
- Stage 3: Sepal primordia start to form. The abaxial sepal (furthest from the centre of the SAM) is the first to start growing, followed by the adaxial sepal (closest to the centre of the SAM), and lastly, the two lateral sepals.
- Stage 4: The sepal primordia are clearly formed and begin to cover the flower primordia's central dome (the FM). The order of sepal growth is the same as in stage 3.

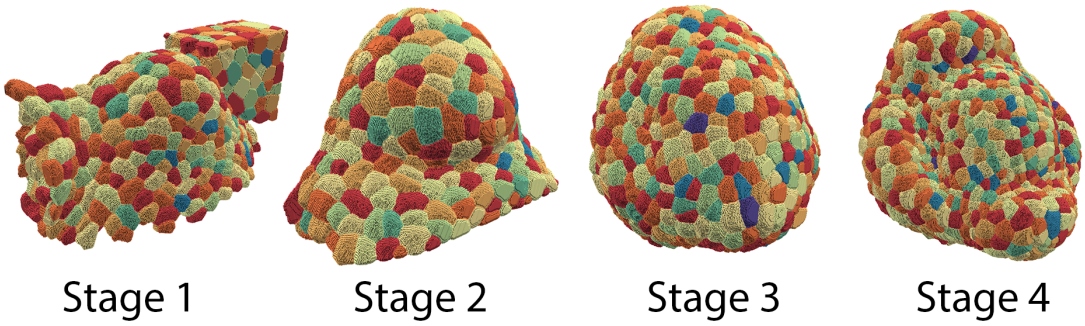

Figure 2: In stage 1, a small outgrowth can be seen forming on the SAM, and in stage 2, a clear groove has formed between the flower primordium and the SAM. In stage 3, the flower primordia are no longer spherical; rather, the four sepals can be seen forming. When stage 4 is reached, the sepals can very easily be identified. In stage 1 and stage 2, parts of the SAM can still be seen, whereas the SAM has been excluded for the plots of stage 3 and stage 4.

2.1.1 Auxin and PIN

An important class of plant hormones are auxins, with the most abundant native auxin being indole-3-acetic acid (IAA). The hormone has been studied for a long time, with behaviours such as plant stems bending towards light sources (positive phototropism) described by Darwin[26]. Auxin has been described to have essential roles in root initiation, cell division, vascular tissue differentiation, and flower growth[27, 28, 29]. Although it has been possible to indirectly image auxin on a cellular scale during the last two decades using reporters such as DR5rev::GFP[30, 31], it was not until very recently possible to directly image auxin on a subcellular level[32].

With better techniques available for imaging and quantifying important hormones like auxin, new possibilities open up for computational models, with a subset of models being auxin transport models. Published transport models have used passive influx and efflux

combined with active influx and efflux, where the active flux is determined by the concentration of transport proteins in the cell membranes. One such family of proteins responsible for the active efflux of auxin is PIN-FORMED(PIN)[33]. Most PINs are asymmetrically distributed across the cell membranes, which leads to cell polarity and directionality of the auxin transport. Cell polarity is an essential characteristic for polarised cell growth, asymmetric cell divisions, directional nutrient transport, and hormone gradients across tissues[34]. Another family of proteins, which are responsible for the active influx, is AUX and LAX (Like-AUX)[35], where AUX1 is a well-studied member[36].

Polarised auxin transport models based on PIN1[37] abundance in the cell membranes have been able to show the formation of auxin peaks in the SAM[38] as well as auxin distributions throughout the roots, leaves, and stems[39] in *Arabidopsis thaliana*.

However, an issue that complicates the optimisation and validation of the auxin transport models and other models that require data from multiple different specimens is that there is no trivial way of compiling all the data in one representative geometry. For example, PIN1 and AUX1 data may be exclusive to different flowers with varying numbers of cells with different cell volumes, slightly different morphology, and different cell neighbours.

2.2 Processing of image data

2.2.1 Confocal microscopy

When imaging 3D tissues with multiple fluorophores, two common approaches are using light sheet and confocal microscopy. Light sheet microscopy is typically more suited for imaging larger tissues such as mouse brains, whereas confocal microscopy is preferable for tissues like flower primordia (order of 100μm) due to its higher resolution[40]. Confocal microscopes work by shining a laser on the sample where the fluorophores then emit light, and through a complex setup of filters and mirrors, the microscope can filter out a thin plane of emitted light. The thin plane is the XY-plane, and by taking images of successive planes along the Z-axis, a stack of images called a Z-stack is created, which forms a 3D representation of the sample (Fig. 3).

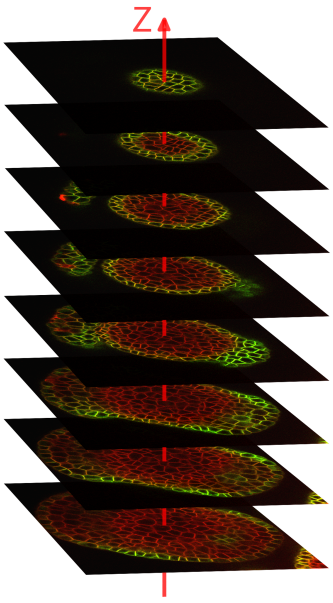

Figure 3: Schematic figure showing the stack of confocal image slices that makes up the final Z-stack. Most of the slices have been excluded to highlight the difference in the image slices. The size of the images considered in this thesis are on the order of 500x500x500 voxels.

2.2.2 Image segmentation

Image segmentation is the process of dividing an image into labelled sub-regions defined by pixel or voxel intensities of an image. There are many different segmentation techniques since different types of analyses require different parts of the images to be segmented[1, 41, 42]. In an image of a tissue where cell membranes have a high pixel intensity, and non-membrane regions have low pixel intensity, the task of the segmentation algorithm is to label each cell and all of its corresponding pixels. A state-of-the-art pipeline for plant cell segmentation called PlantSeg was recently published[43], and is used in this thesis. The segmentation is further explained in section 5.1.

2.3 Image registration

A problem when there are images of two tissues of the same type but with different morphology is that it is hard to make direct comparisons between the images. The process of aligning images is called registration, and an example of a simple registration problem is illustrated in figure 4. The two images during the registration process are called the moving and fixed image, where the moving image is transformed to match the fixed image.

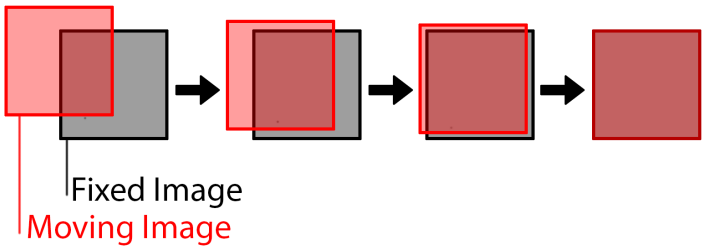

Figure 4: A simple registration could, for example, be iteratively transforming the moving image via translation (Eq. 2.2) and using the mean squared error of the pixel intensities between the moving and the fixed image. Gradient descent can then be used to optimise the registration.

Registration of flower primordia has been done for confocal images of the same primordium but taken at different angles[3] and different flower primordia at different times[44]. However, much of the research about tissue image registration comes from the medical field, with software like Advanced Normalisation Tools (ANTs)[45] and Elastix[46, 47] which both contain optimisations for brain scan registrations, but that also perform well for general image registration problems. In this thesis, a python wrapping for Elastix called SimpleElastix[47] is used for the registrations. Registration of images is helpful for computing statistics in datasets that contain the same type of objects but seen from different angles or which stems from different sources; for example, brain scans from thousands of patients[48].

2.3.1 Mutual information

A primary metric often used in the registration algorithm is mutual information[49]. The details of the metric will not be discussed in detail, but the most straightforward explanation is that it is a measure of the similarity between two images. Mutual information, $I(X;Y)$, can be described as how much information one knows about the random variable X, given information about the random variable Y. In the case of mutual information between two images X and Y, pixels are sampled from both images, which forms a joint probability distribution, $P_{XY}(x,y)$, where x and y are pixel intensities. $I(X;Y)$ is then defined by:

$$I(X;Y) = \sum_{x,y} P_{XY}(x,y) \log\left(\frac{P_{XY}(x,y)}{P_X(x)P_Y(y)}\right)$$

Where $P_X(x)$ and $P_Y(y)$ are the marginal probability distributions:

$$P_X(x) = \sum_y P_{XY}(x,y) \ , \qquad P_Y(y) = \sum_x P_{XY}(x,y)$$

Another intuitive explanation comes from another formulation of mutual information (Eq. 2.1)[50]. If X is unknown information, Y is known information, $H(X)$ is the uncertainty about X, and $H(X|Y)$ is the uncertainty about X given that we already know Y. If the uncertainty is the same whether we know Y or not, i.e. $H(X) = H(X|Y)$, then there is no mutual information between X and Y; thus $I(X;Y) = 0$.

$$I(X;Y) = H(X) - H(X|Y) \tag{2.1}$$

2.3.2 Transformations for registration

Typical transformations that are used for registration can be described by transformation matrices (M_x) and are translation ($M_{translation}$, Eq. 2.2), rotation ($M_{rotate\ x}$, Eq. 2.3), scaling (M_{scale}, Eq. 2.4), and shearing ($M_{shear\ x}$, Eq. 2.5). The rotational and shearing matrix are only shown for transformations along the x-axis, but similar matrices exist for the y-axis and z-axis.

$$M_{translation} = \begin{pmatrix} 1 & 0 & 0 & T_x \\ 0 & 1 & 0 & T_y \\ 0 & 0 & 1 & T_z \\ 0 & 0 & 0 & 1 \end{pmatrix} \tag{2.2}$$

$$M_{rotate\ x} = \begin{pmatrix} 1 & 0 & 0 & 0 \\ 0 & \cos(\theta) & -\sin(\theta) & 0 \\ 0 & -\sin(\theta) & \cos(\theta) & 0 \\ 0 & 0 & 0 & 1 \end{pmatrix} \tag{2.3}$$

$$M_{scale} = \begin{pmatrix} S_x & 0 & 0 & 0 \\ 0 & S_y & 0 & 0 \\ 0 & 0 & S_z & 0 \\ 0 & 0 & 0 & 1 \end{pmatrix} \tag{2.4}$$

$$M_{shear\ x} = \begin{pmatrix} 1 & 0 & 0 & 0 \\ Sh_y & 1 & 0 & 0 \\ Sh_z & 0 & 1 & 0 \\ 0 & 0 & 0 & 1 \end{pmatrix} \tag{2.5}$$

In order to represent translations in matrix form, 4x4 matrices are used such that the transformations can be evaluated as follows:

$$\begin{pmatrix} 1 & 0 & 0 & T_x \\ 0 & 1 & 0 & T_y \\ 0 & 0 & 1 & T_z \\ 0 & 0 & 0 & 1 \end{pmatrix} \begin{pmatrix} x \\ y \\ z \\ 1 \end{pmatrix} = \begin{pmatrix} x + T_x \\ y + T_y \\ z + T_z \\ 1 \end{pmatrix} \tag{2.6}$$

. Sometimes more advanced techniques need to be used due to local deformities in the different images; imagine if the fixed image in figure 4 had a bump on one of the sides. In order to deal with local deformities, a free form deformation technique using B-splines can be used[51]. A simple description of the B-spline registration technique is that a set of underlying points is generated, forming a mesh. By manipulating the underlying mesh, a deformation field can be computed, which can be applied to an image (Fig. 5)

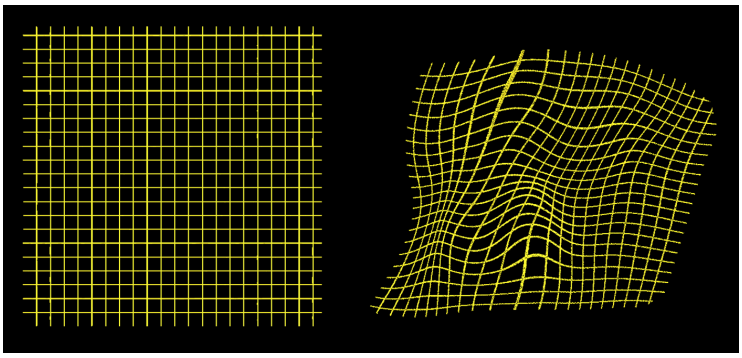

Figure 5: One slice of a 3D grid that is used to visualize the deformation field from a B-Spline registration. On the left side the grid is seen before deformation and on the right side the grid has been warped by the deformation field.

3 Results and Discussion

3.1 Nonlinear registration of tissues can preserve cellular concentrations

A method was developed that aimed to transfer data between tissues of different morphology (Fig. 6). In this thesis, the method is tested on flower primordia from *Arabidopsis thaliana*.

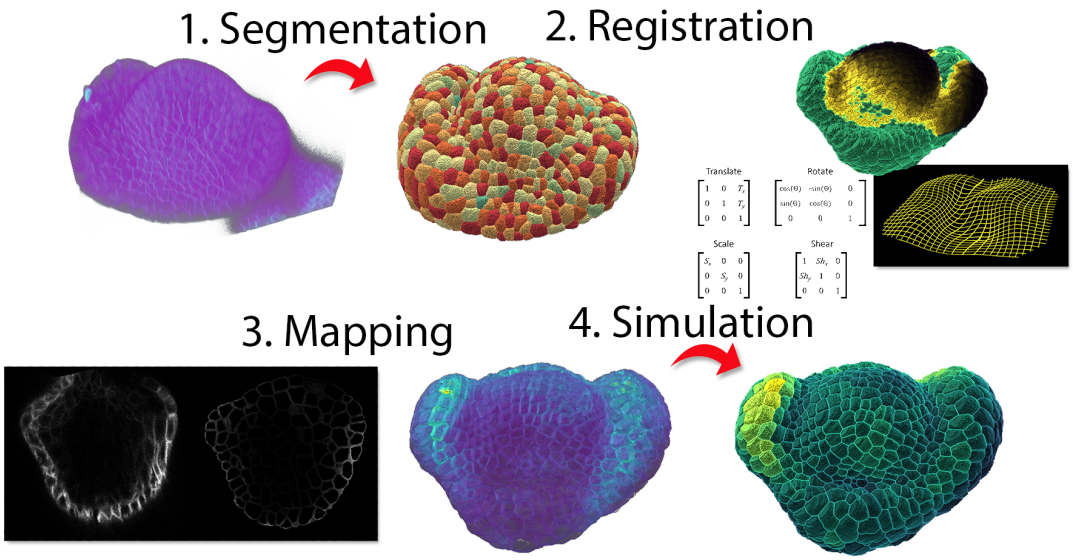

Figure 6: Overview of the steps followed to do the data mapping. During step 3, the novel method, sectorial mean decomposition, is carried out. The general workflow is represented in step 1-3, while step 4 is used in this thesis to evaluate the quality of the mapping.

First, the best matching flower primordia were determined. The fixed images used during the matching are four flower primordia from a recently published atlas[6], while the moving images are from an unpublished data set of seven flower primordia with PIN1 data. To evaluate the similarities between the flowers more quantitatively, a volume metric, M, was defined as:

$$M = \max(1 - \frac{|V_{source} - V_{target}|}{V_{target}}, 0)\,, \tag{3.1}$$

where V_{source} and V_{target} are the two tissues respective volume before registration. By comparing M and manually inspecting the tissues, two flowers were found to be the best candidates to be mapped on the target (Fig. 7). The moving images do not perfectly match the fixed image in terms of their developmental stage since the lateral sepals in the moving images are not sufficiently developed; however, they are sufficiently matched to evaluate the SMD.

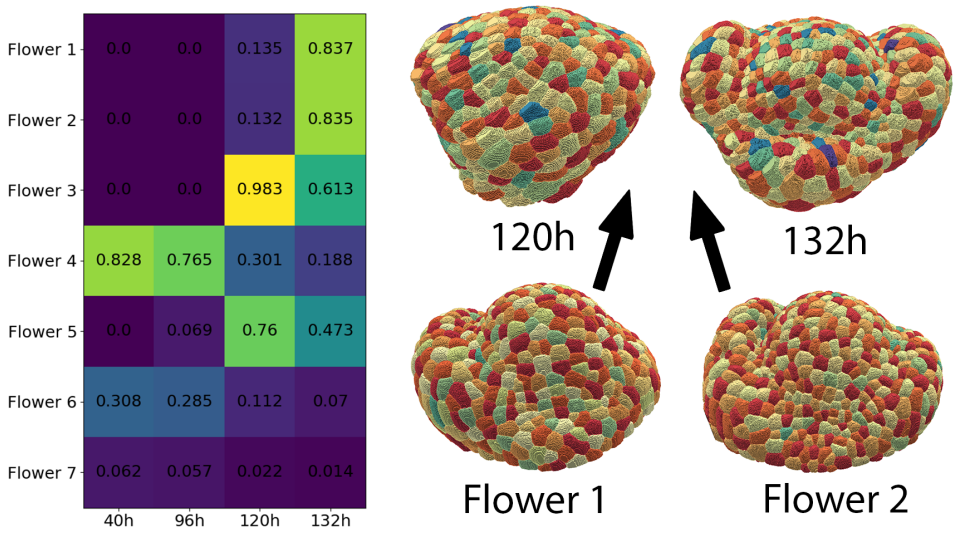

Figure 7: Figure showing the process of choosing matching flowers. On the left side, a volume metric is shown (Eq. 3.1). The metric makes it possible to spot the flowers that might be of a similar developmental stage. Flower 1-7 are the source flowers that are to be mapped to the atlas flower, while 40h-132h are the atlas flowers, named by their age. Flower 1 and 2 are found to have a volume similar to 132h, but when manually inspecting the flowers, their developmental stage appears to be between 120h and 132h. 132h is still chosen to be the best match.

Nonlinear registration was then performed, aligning the two source flowers with the target flower, as illustrated in figure 8. The similarity metric used during the registration is mutual information, which is sufficient to get a good overlap between the images once a distance transform has been applied to the binary images that are used for the registration (Sec. 5.2). A point-based distance metric is also included, using manually picked point-pairs in the moving and fixed image. The distance metric can ensure that the abaxial and adaxial sepals are aligned during the translational, rigid, and affine registration in the case of a flower.

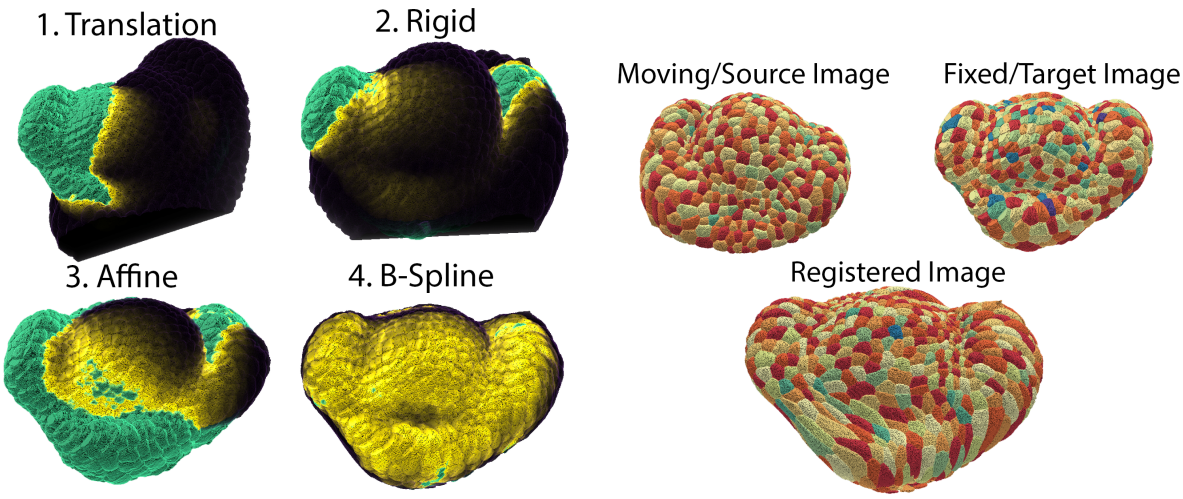

(a) (b)

Figure 8: **(a):** The four steps in the registration process. The overlap between the moving and fixed image is shown as yellow, the fixed image as turquoise, and the moving image as dark translucent violet. **(b):** The registered image is the result of the transformation from (a) applied to the moving/source image. The transformation in (a) was found by registering the moving/source image to the fixed/target image.

For our data mapping method, it is not relevant if a cell is deformed as long as the concentrations of the cells remain the same. Data was collected for the registered tissue pairs to analyse how cell geometries and cell concentrations change during the registration. Following the registration of the source image, some of the cells will have had their geometries changed (Fig. 9a, 8b). While most cells have volumes correlating before and after transformation, a few cells have increased substantially in volume. Still, despite the volume changes, the integrity of the concentration data is shown to be kept by comparing the concentrations in the cells before and after the transformation (Fig. 9b).

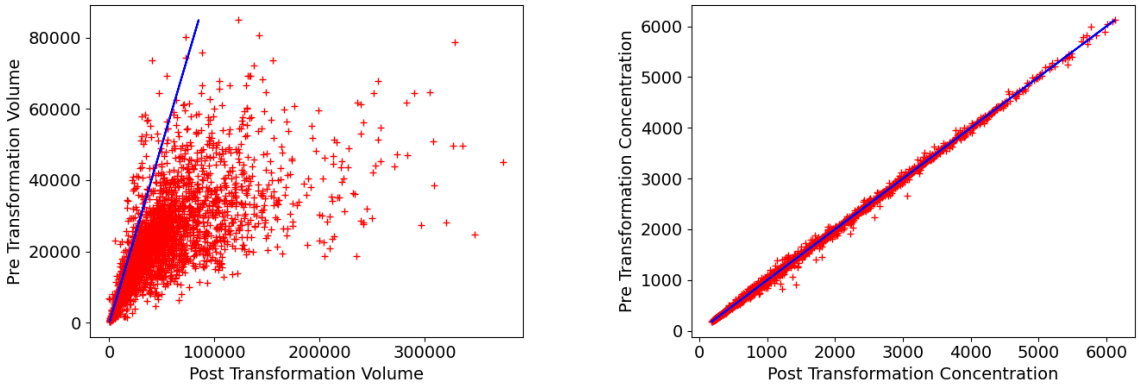

(a) (b)

Figure 9: Comparison of volume and concentration for cells in two source flowers before and after the registration transformation. The concentration is defined as the sum of the PIN1 intensity within one cell divided by the volume. **(a):** Red crosses show the cell volume before and after transformation. The blue line shows $y = x$. **(b):** Red crosses show the total cell concentration before and after transformation. The blue line shows $y = x$. The large outliers in b) were identified to be cells which had most of their volume moved outside of the image after the transformation.

3.2 Sectorial mean decomposition can preserve large scale features of membrane data during data mapping between tissues

To be able to map cellular data between the registered flowers, it is necessary to know which source cells, i, should be mapped to which target cell, j; for this, a simple volume overlap measure, O_{ij}, is used (Sec. 5.3). A fraction is calculated from the intersecting volume between the source and target cell and the volume of the target cell; this fraction will determine how much of the source data should be mapped to each target cell.

Mapping membrane data from one tissue to another requires it to be represented in a new way. To do this, we introduce SMD, which works by decomposing each cell in the source tissue into sectors formed by angular intervals, where all the surface voxels of the sector are set to the mean surface concentration of the sectors (Fig. 10). To exclusively map the membrane data, a border width must be chosen for the SMD. The width is the number of voxels on the interior side of a cell's border with another cell, and by manual inspection, two voxels were chosen for this data set (Fig. 11b). The risk of a too small width is that not enough signal is used for the mapping, and too large width would cause a smoothing effect since the mapped mean would be distorted by either non-membrane bound signals or noise.

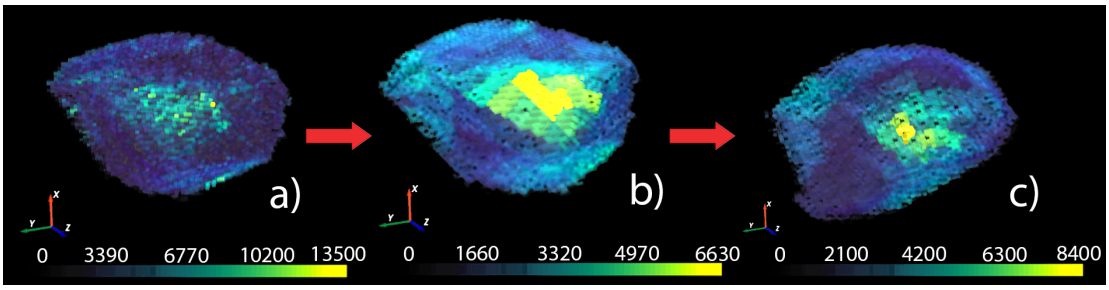

Figure 10: Steps of the sectorial mean decomposition when assuming that their overlap fraction $O_{ij} = 1$. The angular intervals are $\Delta\phi = 11.25°, \Delta\theta = 22.5°$. **a):** Original single cell data. **b):** SMD applied to the cell in a). The sectors are clearly visible but the distribution along the cell surface remains similar. **c):** Sector data from b) recomposed on a different cell geometry.

Following the decomposition of the source cells and the cell overlap calculations, the source data needs to be recomposed in the target tissue. The source cells and target cells are decomposed such that they have the same number of sectors, and the data in the source sectors can be mapped to the target sectors (Eq. 5.10). An example where it is assumed that the overlap fraction $O_{ij} = 1$ is shown in figure 10. By iterating over the source and target cells, the target image is recomposed using the decomposed source data; an example of a slice from the final mapping can be seen in figure 11d.

Initially, the mapping quality may be naively assessed by qualitative inspection. It is clear that large scale features such as the low concentration in the centre of the tissue are preserved (Fig. 11). However, it becomes non-trivial to compare the mapping on a voxel basis since the geometries are different and since there is no ground truth in the target image.

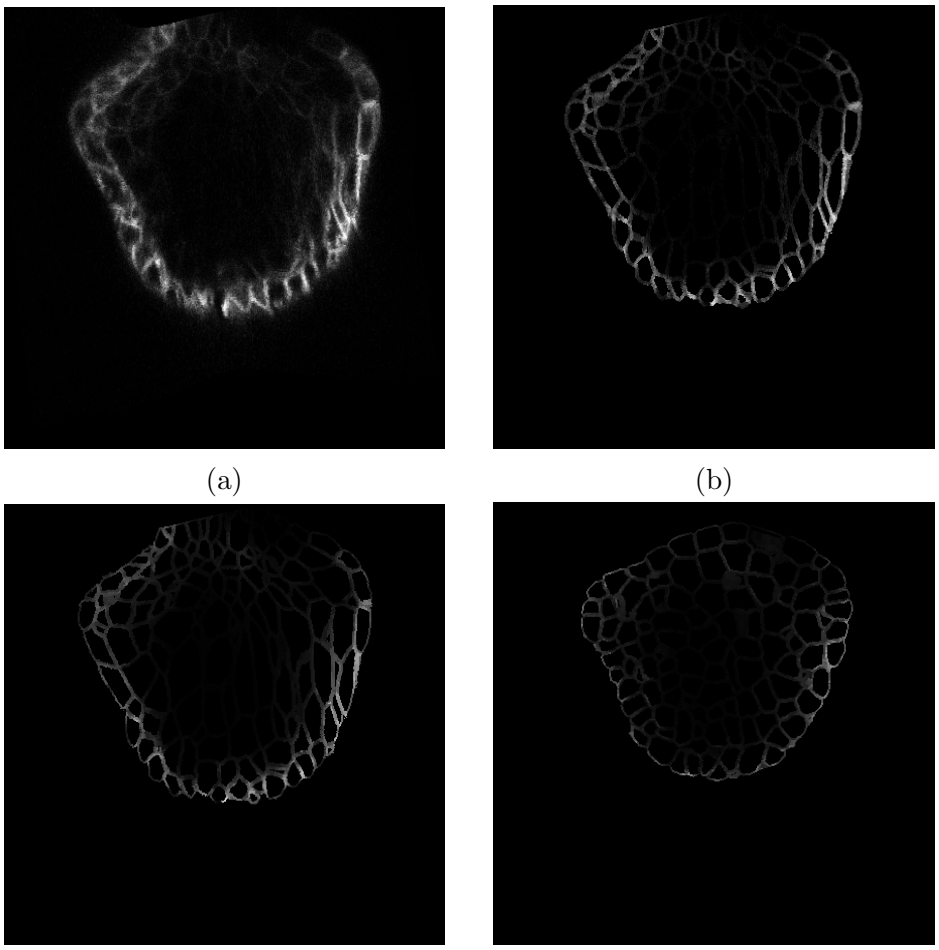

Figure 11: Comparison of the same image slice during different stages of the mapping process. The data is the GFP intensity of the protein PIN1. **(a):** Raw data that has been registered to match a target image. **(b):** Same data as in (a), but filtered to only show two voxels on the sides of each cell membrane. **(c):** Sectorial Mean Decomposition applied to the raw data in (a). **(d):** Decomposed data in (c) mapped to the target image from the registration.

Following the mapping of more than one source image, it becomes easy to compute statistics such as the mean since all the mapped data is in the exact same geometry (Fig. 12). If only one source image is mapped, there is a risk that unwanted features are transferred, especially if the source and target image are in different developmental stages. Having more sources should make the final mapped data more robust.

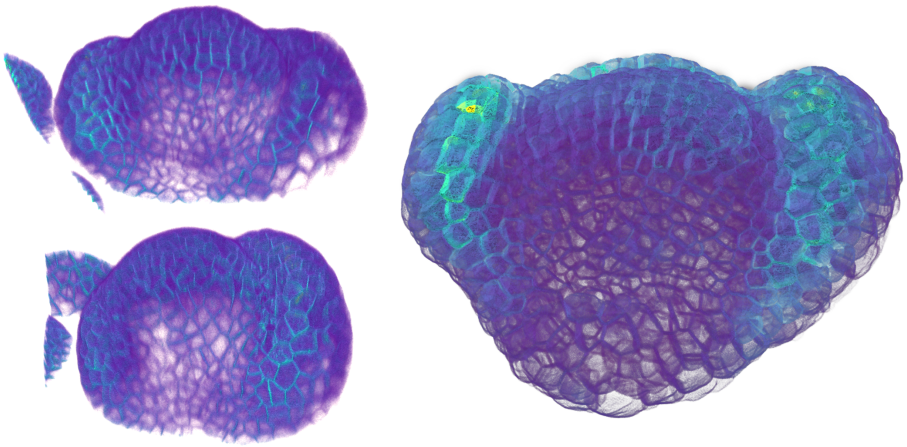

Figure 12: On the left side, the PIN1 data for flower 1 and 2 from figure 7 is shown. On the right side, the average of the mapped PIN1 data from flowers 1 and 2 onto flower 132h from figure 7 is shown. The angular intervals used for the SMD is $\Delta\phi = 22.5°, \Delta\theta = 45°$.

There are other ways to choose which source and target cells should be connected, such as the cells with maximum overlap or the cells with the shortest distances between their centres. However, the overlap measure that has been used in this thesis has a few benefits. Although not utilised in the results shown, it would be easy to include weights between specific cells if the data sets are annotated with cell type or which cell layer they belong to. Using cell layers could ensure that the data from epidermal source cells are mapped with a much higher weight to epidermal target cells.

3.3 Simulation of an auxin transport model can be used to evaluate the quality of membrane data mapping

To evaluate the quality of the membrane data mapping, an auxin transport model is used (Sec. 5.6). The simulations are run until an equilibrium state has been reached, where it is possible to observe if the resulting concentration pattern remains after the mapping. Firstly, the error from the angular sectioning parameter in the SMD is quantified by decomposing and mapping the data to its own geometry. Using the self-mapped data allows comparisons of the cellular concentrations from the simulations before and after the SMD. It is clear that the patterns are maintained with sufficiently small angular intervals (Fig. 13).

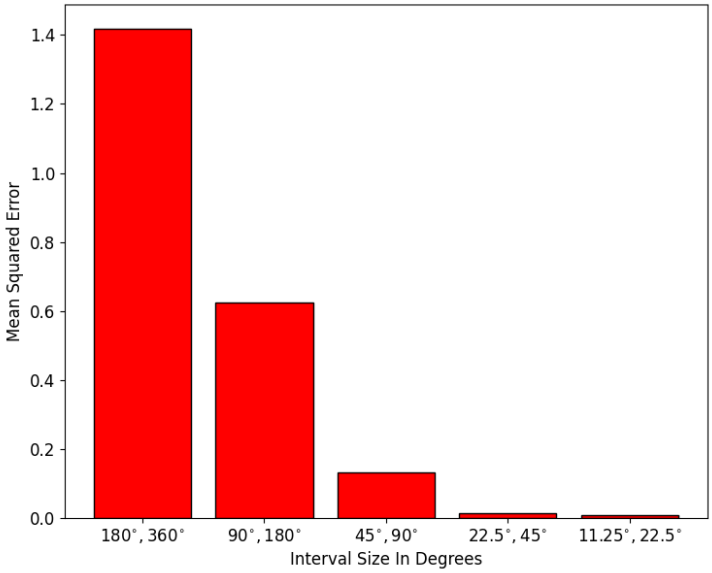

Figure 13: Figure showing the simulation error after the sectorial mean decomposition. The interval $\Delta\phi = 180°, \Delta\theta = 360°$ corresponds to the entire cell surface having the same value, and thus no polarization. The difference between the raw data and the decomposed data becomes small enough to maintain the dynamics of the simulation to a substantial degree at intervals of $\Delta\phi = 22.5°, \Delta\theta = 45°$. The intervals are explained in section 5.4.

Next, the procedure is tested between two flower primordia where PIN1 data is available (Fig. 14). Comparing the equilibrium auxin distribution in the two tissues shows that the polarisation of PIN1 is kept after the mapping to the new geometry since the auxin peaks remain after data mapping (Fig. 14).

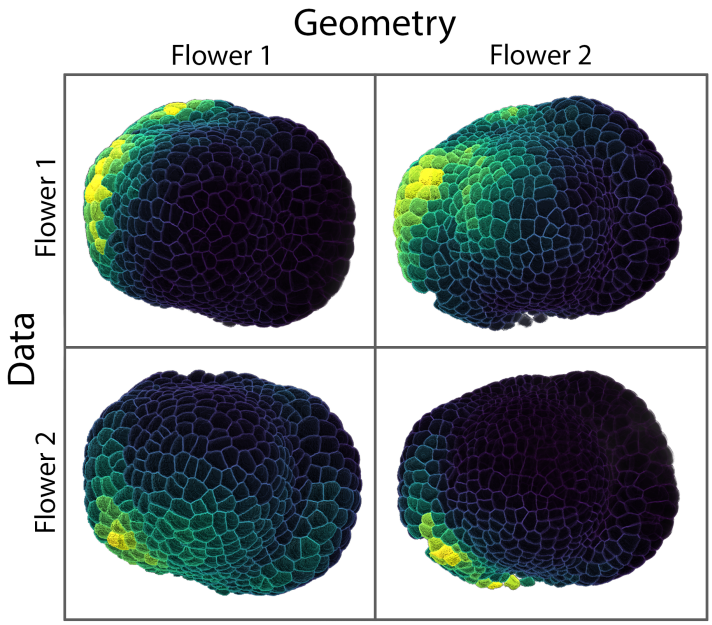

Figure 14: Comparison of the auxin transport simulation results for flower tissues with PIN1 data. The tissue geometry from two flowers is combined with their data to yield four combinations. Along the primary diagonal, the data and geometry come from the same flower. Along the secondary diagonal, the data from the other flower was mapped using SMD with angular intervals of $\Delta\phi = 22.5°, \Delta\theta = 45°$. The general area of high auxin concentration (yellow) is kept after mapping, which indicates that PIN1 is still polarised, but the equilibrium state is slightly more diffused.

Finally, the data mapping from source flower primordia with PIN1 data to an atlas flower primordium without PIN1 data is tested (Fig. 15). The equilibrium pattern is maintained after the mapping as seen if comparing the auxin pattern on the original tissue with the pattern on the target template figure 15a and 15e as well as figure 15c and 15g. The locations of the auxin peaks are preserved to a large degree. When two source flowers have been mapped to the same target flower (Fig. 12), the mapped data can be averaged before the simulation as seen in figure 15i and 15j. With sufficiently many sources, more advanced statistics can be computed, such as which regions have high variability in their concentrations.

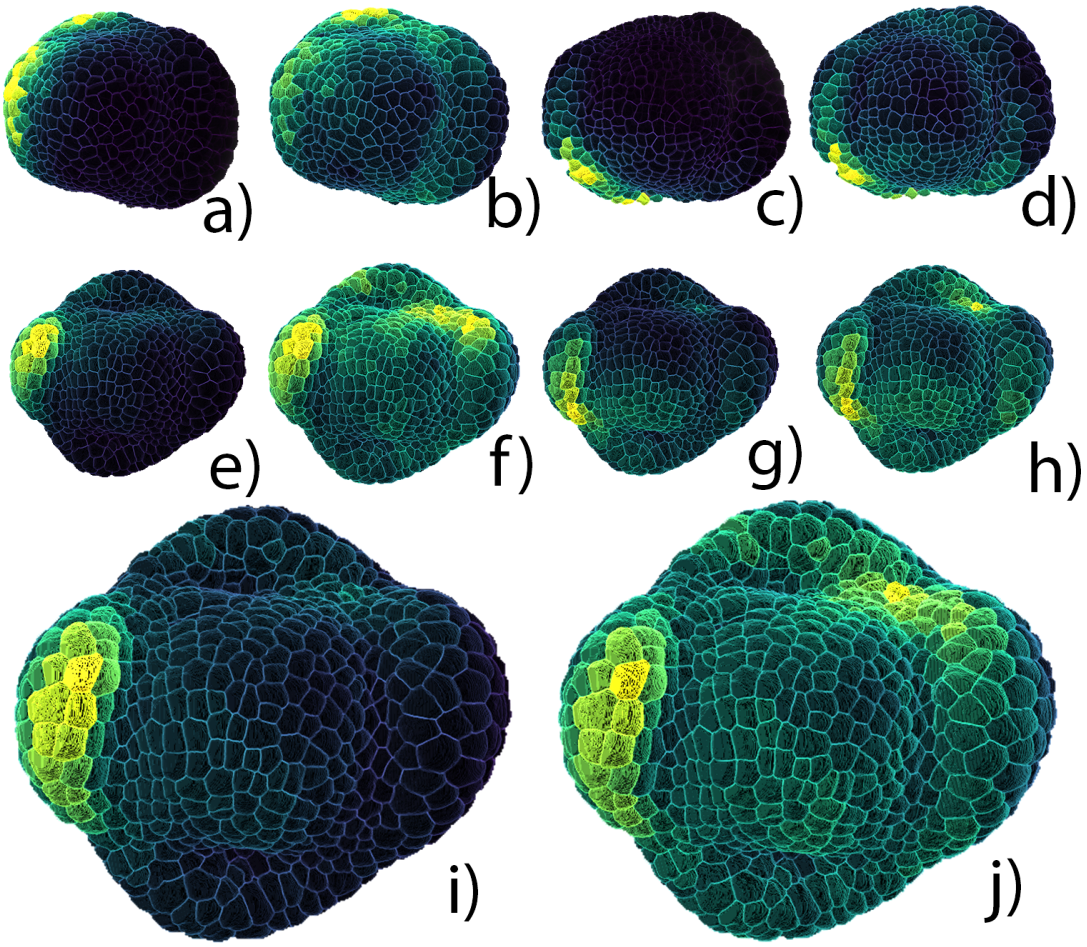

Figure 15: The figure is showing the auxin concentration when the auxin transport model has reached an equilibrium. **a):** Source flower one. **b):** Source flower one with constant auxin production and degradation. **c):** Source flower two. **d):** Source flower two with constant auxin production and degradation. **e):** Source flower one mapped to target flower from the atlas. **f):** Source flower one with constant auxin production and degradation mapped to target flower from the atlas. **g):** Source flower two mapped to target flower from the atlas. **h):** Source flower two with constant auxin production and degradation mapped to target flower from the atlas. **i):** Source flower one and two mapped to target flower from the atlas. **f):** Source flower one and two with constant auxin production and degradation mapped to target flower from the atlas.

4 Conclusion

In this thesis, a novel method for data mapping has been presented and evaluated on flower primordia from *Arabidopsis thaliana*. The method shows much promise since it manages to transfer data between tissues while preserving the distributions of membrane-bound

proteins as evaluated by comparing the equilibrium pattern of an auxin transport model before and after the data mapping.

Although the method was only applied to one tissue type, nothing suggests it is not useful for other tissues with similarly compact arrangements of cells. Once two images have been segmented and registered, and the tissue is dense enough such that cells of the same type are overlapping, the mapping will be trivial. The method is not restricted to plant tissues, and it would work in animal tissues as well, although if the cell shapes are too deviant from a spherical shape, such as in neurons, the angular mapping would need to be replaced.

A potential improvement can be how the source cells are calculated to be connected to the target cells. By first annotating the cells, the mapping can become more specific[10]. With another method of establishing the cell-to-cell correspondence, it could also be unnecessary to register the images. Manual correspondence could, for example, be picked in a tissue with a small number of clearly defined cells. Still, for flower tissues, a direct cell-to-cell correspondence between two flowers does not exist[6].

With a mapping method like the one presented, it is possible to revisit older data sets and recompile them such that they can be used for data quantification and model optimisation, and it could even enable optimisation that was not possible before. This is especially true for models with many molecular species that could not be imaged in the same tissue due to the constraints of how many reporters one can use simultaneously. If enough tissues are combined, it will also be possible to compute the regional variance of the data, which is essential for the development of stochastic models.

5 Method

5.1 Segmentation

Initially, membrane data is used to create an image with segmented and labelled cells; the segmented image is represented as a 3D integer array, where the voxel values are the cell labels, and the background voxels are 0. Another binary 3D array is also created, with 1 being foreground and 0 being background, which will be used for the registration. The images containing the data that is to be mapped are referred to as source or moving images, whereas the images that the data will be mapped to are referred to as target or fixed images.

At this point the data consists of:

- Segmented source images
- Binary foreground/background source images
- Source images containing membrane data

- Segmented target images
- Binary foreground/background target images

The cellular segmentation was done using PlantSeg, a recently developed segmentation pipeline that uses neural networks to improve the accuracy of the segmentation[43]. The steps of the segmentation are as follows:

- Rescale the image to the same size as the images that the neural network was trained on.
- Run the image through a pre-trained neural network, which predicts whether a voxel is a cell boundary or not using a U-net architecture[52] implemented in PyTorch.
- Segment the image using a 3D watershed transform and the multicut segmentation algorithm[53], an algorithm that tries to find the global optimal segmentation.

Most of the default settings are used in PlantSeg except for the following parameters:

- Patch size for neural network: 128x128x128
- Stride for neural network: accurate (64, 64, 64)
- Device Type: CUDA
- 2D watershed: False (corresponds to doing 3D watershed)
- Algorithm: MultiCut

The entire segmentation pipeline takes approximately 30 seconds using a Nvidia RTX 3070 GPU and AMD Ryzen 3900X CPU. After the image has been segmented, the segmented data is manually cleaned such that cells from the surrounding tissue are discarded.

5.2 Registration

Registration was done using SimpleElastix[47], an extension of SimpleITK and a Python wrapping for the popular toolkit Elastix[46]. A visualisation of the registration steps can be seen in figure 8a. Volumetric segmentation data for a source image and a target image is first transformed to binary images, with 0 being background and 1 being tissue/foreground. A distance transform is applied to the binary images such that the voxels furthest away from the edge of the tissue has the largest distance and thus the largest value. The distance transform can also be described as each pixel in the foreground having the value of the distance to the closest edge. The distance transformed image is then normalised by

dividing by the maximum distance. The distance transform gives the registration algorithm more information since it can struggle to find good registration for binary images. The registration is then carried out in four steps:

- Multi-resolution translation registration.
- Multi-resolution rigid (translation and rotation) registration.
- Multi-resolution affine (rotation, translation, scaling, shearing) registration.
- Single-resolution B-Spline (non-rigid) registration.

The Multi-resolution registration is done at different resolutions, starting with the lowest resolution and then propagating the transformation for higher resolutions. It is advantageous to start at a low resolution to avoid local minima if the source and target tissue have significant differences in their initial position and orientation. The Single-resolution B-Spline registration is done directly on the highest resolution images. For the optimisation, an adaptive stochastic gradient descent method is used with mutual information as a metric. Matching points of interest are manually picked in the moving and fixed image to ensure proper registration during the translation, rigid, and affine registration. In this thesis, seven pairs of points are manually picked to ensure that the sepals are aligned correctly. The points locations are the peaks of the abaxial and adaxial sepals, the grooves between the sepals and the central FM dome, and the peak of the central FM dome.

Once the optimal transformation matrix and deformation field have been found, they are applied to the segmentation image and its corresponding data. It is essential to use a nearest neighbour interpolator for the segmentation image to avoid edge artefacts between the segmented cells since other interpolators would change the segmentation labels.

5.3 Overlap measure

To relate which source cells should map to a target cell, the spatial overlap for the cells is calculated as follows:

$$O_{ij} = \frac{V_i \cap V_j}{V_j}\,, \tag{5.1}$$

where $V_i \cap V_j$ is the volume of the intersection between source cell i and target cell j (Fig. 16). The volume of the intersection is then divided by the volume of the target cell j, which yields the fractional cell overlap, O_{ij}. To make sure that target cells with a total fractional overlap less than one do not get a disproportionately low amount of mapped signal, the following condition is imposed:

$$\sum_i O_{ij} = 1 \tag{5.2}$$

The normalised overlap fractions then become:

$$O_{ij} = \frac{\frac{V_i \cap V_j}{V_j}}{\sum_i \frac{V_i \cap V_j}{V_j}} \tag{5.3}$$

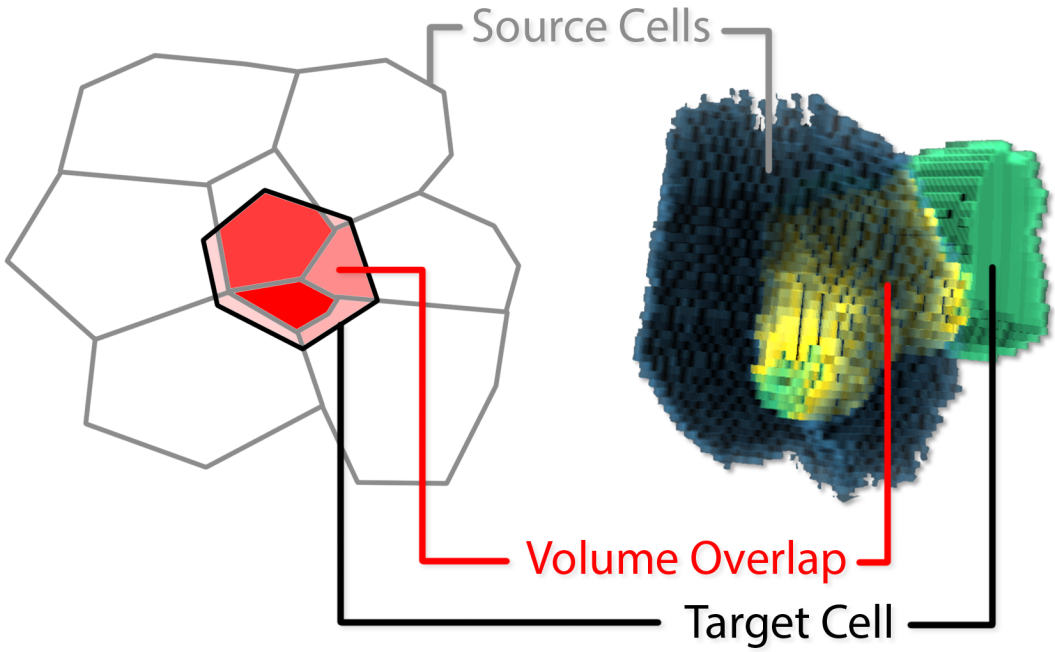

Figure 16: To the left a 2D schematic drawing of the overlap calculation is shown. The opacity of the red colour shows the fractional overlap, O_{ij}. To the right a 3D example is shown with a source cell and a target cell with some of their volume overlapping.

5.4 Sectorial mean decomposition

Initially, the segmented cells are represented as integer labels in the image. The different labels can create a binary mask of all cell borders using a structuring element, such as a ball with a fixed radius. The radius of the ball will be chosen to match the thickness of the cell membranes such that the binary border mask can be used to filter out all the data that is not membrane-bound.

The source cells i and the target cells j are split up into sectors s. The sectors are formed by angular intervals of θ and ϕ in spherical coordinates (Fig. 17). One basic split could be:

- $s_1 = 0° < \theta < 360°, 0° < \phi < 90°$
- $s_2 = 0° < \theta < 360°, 90° < \phi < 180°$

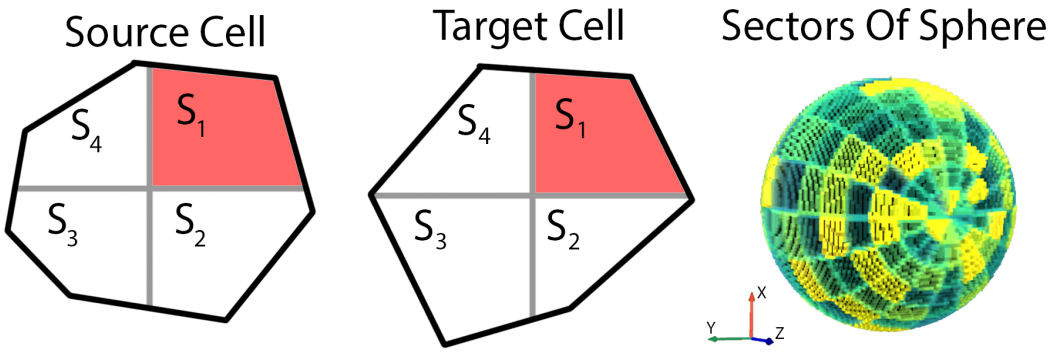

Figure 17: The source and target cell shows how even if the geometries of the cells are different, they can both be divided into linked sectors formed by angular intervals. Furthest to the right an example sphere has been divided into sectors to show how the sectors look in 3D.

Within these sectors, it is assumed that the concentration along the cell membrane will be the same in the source cell and the target cell:

$$c_{sj} = c_{si} \tag{5.4}$$

This can be written as the sum of the voxel intensities along the surface divided by the surface area:

$$\frac{\sum_l P_{js}(l)}{A_{js}} = \frac{\sum_k P_{is}(k)}{A_{is}} \tag{5.5}$$

Since the sum of the voxel intensities is the same as the sum of the mean of the voxel intensities:

$$\sum_l x(l) = \sum_l \bar{x} \tag{5.6}$$

Rewriting equation 5.5 with equation 5.6:

$$\frac{\sum_l \bar{P}_{js}}{A_{js}} = \frac{\sum_k \bar{P}_{is}}{A_{is}} \tag{5.7}$$

Since all elements in the sum are the same we can multiply by the number of voxels:

$$\frac{l\bar{P}_{js}}{A_{js}} = \frac{k\bar{P}_{is}}{A_{is}} \tag{5.8}$$

Moving the areas and numbers to one side we get expression for the voxel intensities in the target cell:

$$\bar{P}_{js} = \frac{kA_{js}}{lA_{is}}\bar{P}_{is} \tag{5.9}$$

Finally, the normalized overlap fraction (Eq. 5.3), is combined with equation 5.9:

$$\bar{P}_{js} = O_{ij}\frac{kA_{js}}{lA_{is}}\bar{P}_{is} \tag{5.10}$$

An example where SMD is applied to the source cell's own geometry is shown in figure 18, where four different angular intervals are shown. In the case where the source and target tissue have the same geometry, the sectors voxels are set to the mean of the voxels in the sector.

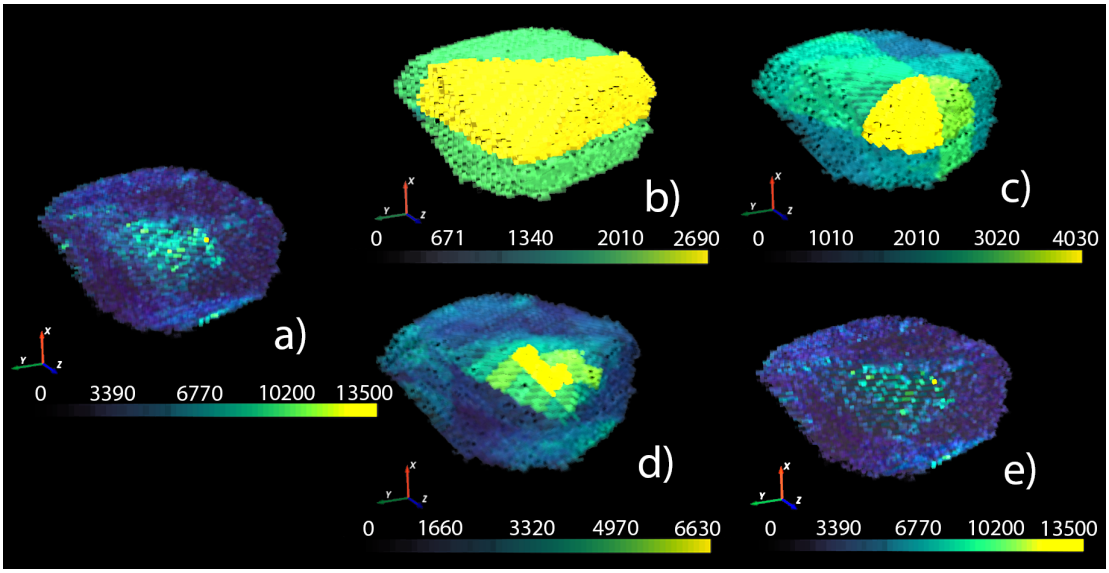

Figure 18: **a):** Original single-cell data. **b):** SMD applied to the cell in a) with angular intervals of $\Delta\phi = 90°, \Delta\theta = 180°$. **c):** SMD applied to the cell in a) with angular intervals of $\Delta\phi = 45°, \Delta\theta = 90°$. **d):** SMD applied to the cell in a) with angular intervals of $\Delta\phi = 11.25°, \Delta\theta = 22.5°$. **e):** SMD applied to the cell in a) with angular intervals of $\Delta\phi = 1°, \Delta\theta = 2°$.

5.5 Quantification of membrane-bound protein

The quantification script used is based on a python package developed for transforming image data to simulations files[54] with a slight modification to enable multi-threading and include normalisation. The script iterates through the cells, i, and their neighbours, j, where the membrane concentration is computed for the shared area between the cell and its neighbour. The shared area, A_{ij}, is computed using a marching cubes algorithm[55] to create a mesh that gives the area. The volume, V_i, is calculated by summing the number of voxels in the cell.

Since the simulation described in the section below requires both PIN1, P, and AUX/LAX, X, and the data on hand is limited to only PIN1, the AUX/LAX concentrations will be guessed depending on the concentration of PIN1 in the corresponding cell. The set of voxels, v, pertaining to one cell is denoted by C_i, the set of voxels pertaining to all the cells walls is denoted by W_i, and the voxels for one of the cells walls shared with the neighbour j by W_{ij}. The voxel intensity in the PIN1 data is denoted by $I_P(v)$. To assign voxels to the walls, a wall depth is chosen. For the quantification done in this thesis, the wall depth was chosen to be two voxels, which means that if $v \in C_i$ and v is within two voxels of the cell membrane, then $v \in W_i$. The quantification is then done as follows, where the unnormalised concentrations are denoted with a tilde sign:

$$\tilde{P}_{total,i} = \sum_v \frac{I_P(v)}{V_i}, \quad v \in C_i$$

$$\tilde{P}_{ij} = \sum_v \frac{I_P(v)}{A_{ij}}, \quad v \in W_{ij}$$

$$\tilde{X}_{ij} = \frac{\sum_v I_P(v)}{\sum_j A_{ij}}, \quad v \in W_i$$

The normalization factor, N, is then computed such that the average PIN1 concentration in each cell is one:

$$N = \frac{1}{n} \sum_i^n \tilde{P}_{total,i}$$

$$P_{total,i} = \frac{\tilde{P}_{total,i}}{N}$$

$$P_{ij} = \frac{\tilde{P}_{ij}}{N}$$

$$X_{ij} = \frac{\tilde{X}_{ij}}{N}$$

5.6 Simulation of auxin transport model

The simulations are computed using the CellCellAuxinTransport function from the software Organism[56]. The method used assumes that the two transporters AUX/LAX (X) and PIN1 (P) remain constant, and the only changing concentration is auxin (a). The passive fluxes are determined by D_{in} and D_{out} while the active transport is determined by T_{in} and T_{out}. Auxin is actively transported out from the cells i by P_{ij} and in by X_{ij}. Some simulations are run with constant production ($\alpha = 0.01$) and constant degradation ($\beta = 0.01$), which is indicated in the affected figures. The contact area between cell i and neighbour cell j is denoted as A_{ij}, and the volume as V_i. The final rate of the auxin concentration in cell i is achieved by summing over all neighbour cells j. The fluxes and the final auxin rate equation is shown in equation 5.11-5.14. The model parameters[38] are seen in table 1.

$$\phi_{out} = \frac{(D_{out} + T_{out}X_{ji})(D_{in} + T_{in}P_{ij})}{2D_{out} + T_{out}(X_{ij} + X_{ij})}a_i \tag{5.11}$$

$$\phi_{in} = \frac{(D_{out} + T_{out}X_{ij})(D_{in} + T_{in}P_{ji})}{2D_{out} + T_{out}(X_{ij} + X_{ij})}a_j \tag{5.12}$$

$$\phi_{ij} = A_{ij}(\phi_{in} - \phi_{out}) \tag{5.13}$$

$$\frac{da_i}{dt} = \sum_j \frac{\phi_{ij}}{V_i} + \alpha - \beta \tag{5.14}$$

Table 1: Parameters for polarized auxin transport model.

Parameter	Value	Unit
D_{out}	$2.20 \cdot 10^{-3}$	μm s^{-1}
T_{out}	1.26	μm M^{-1} s^{-1}
D_{in}	$1.32 \cdot 10^{-1}$	μm s^{-1}
T_{in}	1.96	μm M^{-1} s^{-1}

Acknowledgments

I would like to give my greatest thanks to my supervisors Henrik Jönsson, Henrik Åhl, and Argyris Zardilis, for all the great discussions. Although we were limited to zoom meetings, it worked surprisingly well. I would also like to thank Victor Olariu for his valuable feedback at the start of the semester and during the mid-term presentation. Henrik Åhl also receives an extra thank you due to the data he provided, without which the thesis would not have been possible. And, of course, a thank you to my sambo Maggie for always being there, especially during a crazy year like the one that has just passed.

References

[1] R. M. Haralick and L. G. Shapiro, "Image segmentation techniques," *Computer Vision, Graphics, and Image Processing*, vol. 29, no. 1, pp. 100–132, 1985.

[2] C. D. Whitewoods and E. Coen, "Growth and development of three-dimensional plant form," *Current Biology*, vol. 27, no. 17, pp. R910–R918, 2017.

[3] R. Fernandez, P. Das, V. Mirabet, E. Moscardi, J. Traas, J.-L. Verdeil, G. Malandain, and C. Godin, "Imaging plant growth in 4D: robust tissue reconstruction and lineaging at cell resolution," *Nature Methods*, vol. 7, no. 7, p. 547, 2010.

[4] J. Gunawardena, "Models in biology:'accurate descriptions of our pathetic thinking'," *BMC biology*, vol. 12, no. 1, pp. 1–11, 2014.

[5] H. Jönsson, J. Gruel, P. Krupinski, and C. Troein, "On evaluating models in computational morphodynamics," *Current Opinion in Plant Biology*, vol. 15, no. 1, pp. 103–110, 2012.

[6] Y. Refahi, A. Zardilis, G. Michelin, R. Wightman, B. Leggio, J. Legrand, E. Faure, L. Vachez, A. Armezzani, A.-E. Risson, *et al.*, "A multiscale analysis of early flower development in *Arabidopsis* provides an integrated view of molecular regulation and growth control," *Developmental Cell*, vol. 56, no. 4, pp. 540–556, 2021.

[7] L. Guignard, U.-M. Fiúza, B. Leggio, J. Laussu, E. Faure, G. Michelin, K. Biasuz, L. Hufnagel, G. Malandain, C. Godin, *et al.*, "Contact area–dependent cell communication and the morphological invariance of ascidian embryogenesis," *Science*, vol. 369, no. 6500, 2020.

[8] F. Long, H. Peng, X. Liu, S. K. Kim, and E. Myers, "A 3D digital atlas of C. elegans and its application to single-cell analyses," *Nature Methods*, vol. 6, no. 9, pp. 667–672, 2009.

[9] S. Y. Rhee, K. D. Birnbaum, and D. W. Ehrhardt, "Towards building a plant cell atlas," *Trends in Plant Science*, vol. 24, no. 4, pp. 303–310, 2019.

[10] T. Montenegro-Johnson, S. Strauss, M. D. Jackson, L. Walker, R. S. Smith, and G. W. Bassel, "3DCellAtlas Meristem: a tool for the global cellular annotation of shoot apical meristems," *Plant Methods*, vol. 15, no. 1, pp. 1–9, 2019.

[11] K. V. Thimann and C. L. Schneider, "Differential growth in plant tissues," *American Journal of Botany*, pp. 627–641, 1938.

[12] C. A. Esmon, U. V. Pedmale, and E. Liscum, "Plant tropisms: providing the power of movement to a sessile organism," *International Journal of Developmental Biology*, vol. 49, no. 5-6, pp. 665–674, 2004.

[13] C. A. Esmon, A. G. Tinsley, K. Ljung, G. Sandberg, L. B. Hearne, and E. Liscum, "A gradient of auxin and auxin-dependent transcription precedes tropic growth responses," *Proceedings of the National Academy of Sciences*, vol. 103, no. 1, pp. 236–241, 2006.

[14] J. Van Overbeek, "Phototropism," *The Botanical Review*, vol. 5, no. 12, p. 655, 1939.

[15] Frédéric B., "2018_Arabidopsis_flowering_plant." `https://figshare.com/articles/figure/2018_Arabidopsis_flowering_plant/7159937`, 2018. [Online; accessed May 14, 2021. Licence: `https://creativecommons.org/licenses/by/4.0/legalcode`].

[16] R. A. Kerstetter and S. Hake, "Shoot meristem formation in vegetative development," *The Plant Cell*, vol. 9, no. 7, p. 1001, 1997.

[17] D. R. Smyth, J. L. Bowman, and E. M. Meyerowitz, "Early flower development in *Arabidopsis*," *The Plant Cell*, vol. 2, no. 8, pp. 755–767, 1990.

[18] E. M. Meyerowitz, "*Arabidopsis thaliana*," *Annual Review of Genetics*, vol. 21, no. 1, pp. 93–111, 1987.

[19] M. G. Heisler, C. Ohno, P. Das, P. Sieber, G. V. Reddy, J. A. Long, and E. M. Meyerowitz, "Patterns of auxin transport and gene expression during primordium development revealed by live imaging of the *Arabidopsis* inflorescence meristem," *Current Biology*, vol. 15, no. 21, pp. 1899–1911, 2005.

[20] Y. Cheng and Y. Zhao, "A role for auxin in flower development," *Journal of Integrative Plant Biology*, vol. 49, no. 1, pp. 99–104, 2007.

[21] D. Weigel, J. Alvarez, D. R. Smyth, M. F. Yanofsky, and E. M. Meyerowitz, "LEAFY controls floral meristem identity in *Arabidopsis*," *Cell*, vol. 69, no. 5, pp. 843–859, 1992.

[22] V. F. Irish and I. M. Sussex, "Function of the apetala-1 gene during *Arabidopsis* floral development," *The Plant Cell*, vol. 2, no. 8, pp. 741–753, 1990.

[23] J. L. Bowman, J. Alvarez, D. Weigel, E. M. Meyerowitz, and D. R. Smyth, "Control of flower development in *Arabidopsis thaliana* by APETALA1 and interacting genes," *Development*, vol. 119, no. 3, pp. 721–743, 1993.

[24] E. A. Schultz and G. W. Haughn, "Genetic analysis of the floral initiation process (FLIP) in *Arabidopsis*," *Development*, vol. 119, no. 3, pp. 745–765, 1993.

[25] E. Huala and I. M. Sussex, "LEAFY interacts with floral homeotic genes to regulate *Arabidopsis* floral development," *The Plant Cell*, vol. 4, no. 8, pp. 901–913, 1992.

[26] C. Darwin, *The power of movement in plants*. Appleton, 1897.

[27] P. J. Davies, "The plant hormones: their nature, occurrence, and functions," in *Plant hormones*, pp. 1–15, Springer, 2010.

[28] T. A. Enders and L. C. Strader, "Auxin activity: Past, present, and future," *American Journal of Botany*, vol. 102, no. 2, pp. 180–196, 2015.

[29] S. Paque and D. Weijers, "Q&a: Auxin: the plant molecule that influences almost anything," *BMC Biology*, vol. 14, no. 1, pp. 1–5, 2016.

[30] J. Friml, A. Vieten, M. Sauer, D. Weijers, H. Schwarz, T. Hamann, R. Offringa, and G. Jürgens, "Efflux-dependent auxin gradients establish the apical–basal axis of *Arabidopsis*," *Nature*, vol. 426, no. 6963, pp. 147–153, 2003.

[31] B. Pařízková, M. Pernisová, and O. Novák, "What has been seen cannot be unseen—detecting auxin in vivo," *International Journal of Molecular Sciences*, vol. 18, no. 12, p. 2736, 2017.

[32] O. Herud-Sikimić, A. C. Stiel, M. Kolb, S. Shanmugaratnam, K. W. Berendzen, C. Feldhaus, B. Höcker, and G. Jürgens, "A biosensor for the direct visualization of auxin," *Nature*, pp. 1–5, 2021.

[33] P. Křeček, P. Skpa, J. Libus, S. Naramoto, R. Tejos, J. Friml, and E. Zažímalová, "The PIN-FORMED (PIN) protein family of auxin transporters," *Genome Biology*, vol. 10, no. 12, pp. 1–11, 2009.

[34] A. Muroyama and D. Bergmann, "Plant cell polarity: creating diversity from inside the box," *Annual Review of Cell and Developmental Biology*, vol. 35, pp. 309–336, 2019.

[35] B. Péret, K. Swarup, A. Ferguson, M. Seth, Y. Yang, S. Dhondt, N. James, I. Casimiro, P. Perry, A. Syed, *et al.*, "AUX/LAX genes encode a family of auxin influx transporters that perform distinct functions during *Arabidopsis* development," *The Plant Cell*, vol. 24, no. 7, pp. 2874–2885, 2012.

[36] Y. Yang, U. Z. Hammes, C. G. Taylor, D. P. Schachtman, and E. Nielsen, "High-affinity auxin transport by the AUX1 influx carrier protein," *Current Biology*, vol. 16, no. 11, pp. 1123–1127, 2006.

[37] L. Gälweiler, C. Guan, A. Müller, E. Wisman, K. Mendgen, A. Yephremov, and K. Palme, "Regulation of polar auxin transport by AtPIN1 in *Arabidopsis* vascular tissue," *Science*, vol. 282, no. 5397, pp. 2226–2230, 1998.

[38] H. Jönsson, M. G. Heisler, B. E. Shapiro, E. M. Meyerowitz, and E. Mjolsness, "An auxin-driven polarized transport model for phyllotaxis," *Proceedings of the National Academy of Sciences*, vol. 103, no. 5, pp. 1633–1638, 2006.

[39] P. Krupinski and H. Jönsson, "Modeling auxin-regulated development," *Cold Spring Harbor Perspectives in Biology*, vol. 2, no. 2, p. a001560, 2010.

[40] P. A. Santi, "Light sheet fluorescence microscopy: a review," *Journal of Histochemistry & Cytochemistry*, vol. 59, no. 2, pp. 129–138, 2011.

[41] N. R. Pal and S. K. Pal, "A review on image segmentation techniques," *Pattern Recognition*, vol. 26, no. 9, pp. 1277–1294, 1993.

[42] D. L. Pham, C. Xu, and J. L. Prince, "Current methods in medical image segmentation," *Annual Review of Biomedical Engineering*, vol. 2, no. 1, pp. 315–337, 2000.

[43] A. Wolny, L. Cerrone, A. Vijayan, R. Tofanelli, A. V. Barro, M. Louveaux, C. Wenzl, S. Strauss, D. Wilson-Sánchez, R. Lymbouridou, *et al.*, "Accurate and versatile 3D segmentation of plant tissues at cellular resolution," *Elife*, vol. 9, p. e57613, 2020.

[44] G. Michelin, Y. Refahi, R. Wightman, H. Jönsson, J. Traas, C. Godin, and G. Malandain, "Spatio-temporal registration of 3D microscopy image sequences of *Arabidopsis* floral meristems," in *2016 IEEE 13th International Symposium on Biomedical Imaging (ISBI)*, pp. 1127–1130, IEEE, 2016.

[45] B. B. Avants, N. Tustison, and G. Song, "Advanced normalization tools (ANTS)," *Insight j*, vol. 2, no. 365, pp. 1–35, 2009.

[46] S. Klein, M. Staring, K. Murphy, M. A. Viergever, and J. P. Pluim, "Elastix: a toolbox for intensity-based medical image registration," *IEEE Transactions on Medical Imaging*, vol. 29, no. 1, pp. 196–205, 2009.

[47] K. Marstal, F. Berendsen, M. Staring, and S. Klein, "SimpleElastix: A user-friendly, multi-lingual library for medical image registration," in *Proceedings of the IEEE conference on computer vision and pattern recognition workshops*, pp. 134–142, 2016.

[48] M. De Groot, M. W. Vernooij, S. Klein, M. A. Ikram, F. M. Vos, S. M. Smith, W. J. Niessen, and J. L. Andersson, "Improving alignment in tract-based spatial statistics: evaluation and optimization of image registration," *Neuroimage*, vol. 76, pp. 400–411, 2013.

[49] C. E. Shannon, *The Mathematical Theory of Communication, by CE Shannon (and Recent Contributions to the Mathematical Theory of Communication), W. Weaver.* University of illinois Press, 1949.

[50] S. Dubnov, "Information dynamics and aspects of musical perception," in *The Structure of Style*, pp. 127–157, Springer, 2010.

[51] D. Rueckert, L. I. Sonoda, C. Hayes, D. L. Hill, M. O. Leach, and D. J. Hawkes, "Nonrigid registration using free-form deformations: application to breast MR images," *IEEE Transactions on Medical Imaging*, vol. 18, no. 8, pp. 712–721, 1999.

[52] O. Ronneberger, P. Fischer, and T. Brox, "U-net: Convolutional networks for biomedical image segmentation," in *International Conference on Medical image computing and computer-assisted intervention*, pp. 234–241, Springer, 2015.

[53] J. H. Kappes, M. Speth, B. Andres, G. Reinelt, and C. Schn, "Globally optimal image partitioning by multicuts," in *International Workshop on Energy Minimization Methods in Computer Vision and Pattern Recognition*, pp. 31–44, Springer, 2011.

[54] H. Åhl, "img2org." `https://gitlab.com/slcu/teamHJ/henrik_aahl/img2org`, 2021.

[55] W. E. Lorensen and H. E. Cline, "Marching cubes: A high resolution 3D surface construction algorithm," *ACM SIGGRAPH Computer Graphics*, vol. 21, no. 4, pp. 163–169, 1987.

[56] H. Jönsson, "Organism." `https://gitlab.com/slcu/teamHJ/Organism`, 2021.